



Cite this: *Environ. Sci.: Atmos.*, 2023, 3, 305

## Sensing atmospheric flows in aquatic environments using a multirotor small uncrewed aircraft system (sUAS)

Javier González-Rocha,<sup>a</sup> Landon Bilyeu,<sup>b</sup> Shane D. Ross,<sup>c</sup> Hosein Foroutan,<sup>d</sup> Stephen J. Jacquemin,<sup>e</sup> Andrew P. Ault,<sup>f</sup> and David G. Schmale, III<sup>b</sup>

New wind sensing technologies are needed to measure atmospheric flows in aquatic environments where hazardous agents may be present and conventional atmospheric sensors are difficult to deploy. Here, we present the application of model-based multirotor sUAS (small uncrewed aircraft system) wind estimation to measure atmospheric flow variations in aquatic environments. Thirty-two sUAS flights were conducted at Grand Lake St. Marys (GLSM), Ohio in August, 2019 to characterize differences in wind profiles (wind speed and wind direction) across onshore and offshore (over the lake) locations 80 m apart. A harmful algal bloom was present in GLSM during the experiment. Fourteen calibration flights were conducted at the same site to validate multirotor sUAS wind estimates hovering next to a sonic anemometer (SA) installed 13 m above ground level. Forty-seven calibration profiles were performed in Blacksburg, Virginia on June 30th, 2020 to validate multirotor sUAS wind estimates obtained in steady ascending vertical flight next to a SoDAR wind profiler. Differences between onshore and offshore wind speed measurements at GLSM increased from morning to afternoon on each day of experiments. Flights performed next to SA and SoDAR instruments also demonstrated multirotor sUAS estimates of wind velocity components  $u$  and  $v$  to have mean absolute error values of  $0.4 \text{ m s}^{-1}$  and  $0.3 \text{ m s}^{-1}$  (hovering) and  $1.2 \text{ m s}^{-1}$  and  $1.5 \text{ m s}^{-1}$  (ascending), respectively. Overall, our findings support further development of multirotor sUAS capabilities for resolving atmospheric flows in aquatic environments.

Received 9th April 2022  
Accepted 12th December 2022

DOI: 10.1039/d2ea00042c

rsc.li/esatmospheres

### Environmental significance

The increased presence of harmful algal blooms in freshwater lakes, rivers, and reservoirs, as well as marine coastal areas and estuaries, poses a threat to wildlife and public health. Understanding how microscale atmospheric flows vary with space and time where land and water interface in aquatic environments is critical for characterizing the atmospheric transport of aerosolized cyanobacteria toxins produced by harmful algal blooms. Our study demonstrates that multirotor small uncrewed aircraft systems (sUAS) can reliably provide high-resolution observations of atmospheric flow variations in aquatic environments where surface heterogeneity is significant. High-fidelity measurements of atmospheric flows in aquatic environments can lead to improved atmospheric transport predictions, giving way to new possibilities for developing advisory systems that are precise, connected, and automated to reduce the number of exposure events for downwind communities.

## 1 Introduction

Multirotor small uncrewed (formerly referred to unmanned) aircraft systems (sUAS) can help obtain *in situ* measurements of microscale (sub-1 km) atmospheric flows in aquatic

environments where natural and artificial topographical features are significant. Measuring how microscale atmospheric flows evolve in complex environments has long remained a challenge due to their natural characteristics.<sup>1–3</sup> Microscale flows vary significantly in space and time due to surface roughness and turbulence induced by shear, inertial, and buoyancy effects.<sup>4</sup> Additionally, deploying meteorological towers, tethered balloons, as well as SoDAR and LiDAR wind profilers to measure atmospheric flow velocity is difficult and costly in complex environments.<sup>5,6</sup> Aerial observations from crewed aircraft are also cost prohibitive and suffer from poor resolution near the Earth's surface.<sup>6</sup> Multirotor sUAS, on the other hand, despite having a lower persistence measuring the

<sup>a</sup>Department of Mechanical Engineering, University of California, Riverside, CA, USA.  
E-mail: javier.gonzalezrocha@ucr.edu

<sup>b</sup>School of Plant and Environmental Sciences, Virginia Tech, Blacksburg, VA, USA

<sup>c</sup>Department of Ocean and Aerospace Engineering, Virginia Tech, Blacksburg, VA, USA

<sup>d</sup>Department of Civil and Environmental Engineering, Virginia Tech, Blacksburg, VA, USA

<sup>e</sup>Wright State University, Lake Campus, Celina, OH, USA

<sup>f</sup>Department of Chemistry, University of Michigan, Ann Arbor, MI, USA



atmosphere, are inexpensive, mobile, portable, and easy to deploy over water and hard-to-access topographies.<sup>7</sup> Therefore, new multirotor sUAS enabled capabilities to measure wind velocity may provide reliable targeted observations for resolving microscale atmospheric flows in aquatic environments.

Before multirotor sUAS were widely available, attempts to measure wind velocity, and other key atmospheric variables, with sUAS relied on fixed-wing model aircraft. Konrad *et al.*<sup>8</sup> instrumented a small platform with small sensors to measure wind speed and atmospheric variables. More recent efforts to enable wind sensing with fixed-wing sUAS have led to the development of direct and indirect methods for sampling wind velocity in the lower atmosphere. Direct methods have mostly involved integrating pitot tube and multi-hole probe air data systems on board fixed-wing sUAS for measuring wind velocity.<sup>6</sup> Indirect methods, on the other hand, have employed fixed-wing aircraft kinematic particle, point mass, and rigid body models of varying sophistication to infer wind velocity.<sup>9–11</sup> Elston *et al.*<sup>12</sup> have developed a comprehensive review of direct and indirect techniques for measuring wind velocity with fixed-wing sUAS.

As with fixed-wing aircraft, efforts to sense wind velocity with multirotor sUAS have led to the development of direct and indirect wind sensing techniques. Numerous studies have integrated a variety of flow sensors on board multirotor sUAS to measure wind velocity while hovering at one or multiple fixed locations.<sup>5,6,13</sup> Some of the flow sensor types considered in these studies include cup, hot-wire, and sonic anemometers;<sup>14–17</sup> pitot tube and multi-hole probe air data systems;<sup>18</sup> and LiDAR.<sup>19</sup> The effectiveness of these techniques for measuring wind velocity have been found to depend on the payload capacity of the host aircraft, and the significance of measurement error produced by propeller downwash and vehicle motion. Indirect wind sensing techniques are sensor free, and instead use vehicle models, of varying sophistication, to infer wind velocity from wind-induced motion disturbances from equilibrium flight. The models that have been used to infer velocity have so far included kinematic particle, point mass, and rigid body models.<sup>4,20–22</sup> Overall, the three models have been found to have a comparable performance measuring the prevailing wind velocity. However, studies performed by González-Rocha *et al.*<sup>4</sup> have found higher-fidelity vehicle models to have an improved performance resolving time-varying wind fluctuations.

More recent work has aimed to expand the wind sensing flight envelop of multirotor sUAS beyond just hovering flight. Both direct and indirect wind sensing techniques have been leveraged to measure wind velocity in vertical steady-ascending flight. Direct approaches for profiling wind velocity have mostly involved sonic anemometers.<sup>5,6,15,23,24</sup> Alternatively, indirect wind profiling methods have involved kinematic particle and rigid-body models. The latter wind sensing technique can be adapted for various ascent rates and could also prove useful for measuring wind fluctuations required to infer atmospheric turbulence.<sup>25–27</sup> Rigid body models have been used to estimate wind velocity in the lower atmosphere ascending at various rates.<sup>25</sup> Efforts to explore the feasibility of employing multirotor sUAS wind sensing capabilities for resolving atmospheric flow variations in aquatic environments are just beginning. For

example, a recent study by González-Rocha *et al.*<sup>7</sup> found that multirotor sUAS wind sensing capabilities can be used to characterize the drift of small and irregularly shaped objects in freshwater and saltwater environments. Bilyeu *et al.*<sup>28</sup> leveraged the same wind sensing technique along with an optical particle size sensor mounted on a separate multirotor platform to monitor airborne particles over two harmful algal blooms in Grand Lake St. Marys and Lake Erie, Ohio. The two studies show that multirotor sUAS have great potential for collecting atmospheric observations in aquatic environments where conventional ground-based sensors are a challenge to deploy.

In this paper, we present the application of multirotor sUAS wind profiling for measuring spatiotemporal variations of flow velocity in complex environments where surface heterogeneity is significant. The specific objectives of our work were to: (1) use the rigid body model based wind sensing techniques developed by González-Rocha *et al.*<sup>4,25</sup> to measure how the horizontal wind velocity varies with height across onshore and offshore locations 80 m apart and (2) test the reliability of multirotor sUAS wind velocity estimates flying next to a two-dimensional (2-D) sonic anemometer and a sound detection and ranging (SoDAR) wind profiler. Results from onshore and offshore measurements and calibration experiments were used to evaluate the effectiveness of multirotor sUAS model-based wind sensing techniques for resolving spatiotemporal variations of wind velocity in aquatic environments.

## 2 Methods and materials

### 2.1 Wind velocity profiling in aquatic environments

**2.1.1 Multirotor sUAS flight operations.** Multirotor sUAS flight operations were conducted in Grand Lake St. Marys (GLSM), Ohio on August 5th and 6th, 2019 from 8:00 to 15:00 EDT (local time) to profile wind speed and wind direction at onshore and offshore locations 80 m apart. A harmful algal bloom was present at GLSM during the experiments.<sup>29</sup> As shown in Fig. 1, wind velocity measurements were first collected 50 m offshore and then 30 m onshore less than 5 minutes apart. At each location, wind velocity was first measured hovering at 10 m above ground level (AGL) for approximately 2 minutes before ascending vertically from 10 m to 100 m AGL at a constant rate of  $1 \text{ m s}^{-1}$ . In total, sixteen flight operations were performed on August 5th. An additional fifteen flight operations were conducted on August 6th. The thirty one sets of wind velocity observations collected between August 5th and 6th were used to determine wind velocity variations across onshore and offshore locations with respect time.

**2.1.2 Multirotor sUAS platform.** The multirotor sUAS employed during field experiments is the off-the-shelf 3DR Solo quadrotor shown in Fig. 2. Platform specifications have been previously described by González-Rocha *et al.*<sup>7,25</sup> Briefly, the quadrotor weighs approximately 1.5 kg with battery and a camera and gimbal system installed. The quadrotor is 25 cm tall and measures 26 cm across the span between diagonal motors. The four thrusters of the quadrotor consist of two pairs of clock-wise and counter-clock 880 K<sub>v</sub> brushless motors and self-tightening propellers whose dimensions are 25 cm ×





**Fig. 1** (a) A schematic of the multirotor sUAS operations performed on August 5th and 6th, 2019 to measure wind variability across onshore and offshore sampling locations at Grand Lake St. Marys, Ohio. (b) An image of the multirotor sUAS hovering flight operations conducted to measure wind velocity at 10 m AGL. (c) An image of multirotor sUAS steady ascending flight operations performed to measure wind velocity from 10 m to 100 m AGL.



**Fig. 2** A close-up image of the multirotor sUAS that was used to measure wind velocity at onshore and offshore locations in Grant Lake St. Marys, Ohio on August 5th and 6th, 2019.

11.4 cm. Additionally, the flight autopilot on board the quadrotor is a Pixhawk 2.1 Green Cube autopilot that runs on ArduCopter open-source software. The sampling rate of the GPS and inertial measurement units that form part of the autopilot's attitude and heading reference system range from 5 Hz to 20 Hz. During flight, the quadrotor was controlled using a hand-held 2.4 GHz radio transmitter with a range of up to 0.5 km. Lastly, the multirotor sUAS flight endurance varied between 10 and 15 minutes, depending on wind conditions and the life cycle of the battery powering the aircraft.

**2.1.3 Wind sensing rigid body model.** Wind velocity estimates were derived from wind-induced perturbations to quadrotor motion using the model-based wind estimation framework developed by González-Rocha *et al.*<sup>4,25</sup> Employing this approach, the vehicle motion is described using a rigid body model. This model describes the aircraft orientation using the conventional roll-pitch-yaw Euler angles ( $\Theta = [\phi, \theta, \psi]^T$ ). The

rotation matrix  $R(\Theta)$  that maps free vectors from the body frame to the inertial frame is

$$R(\Theta) = \begin{pmatrix} c\theta c\psi & c\psi s\theta s\phi - c\phi s\psi & c\psi s\theta c\phi + s\phi s\psi \\ c\theta s\psi & c\phi c\psi + s\theta s\phi s\psi & -s\phi c\psi + s\theta c\phi s\psi \\ -s\theta & c\theta s\phi & c\theta c\phi \end{pmatrix}$$

where  $c^*$  and  $s^*$  are abbreviations for the cosine and sine trigonometric functions, respectively. The kinematic equations are

$$\dot{X} = R(\Theta)v + V_w(X,t) \quad (1)$$

$$\dot{\Theta} = L(\Theta)\omega \quad (2)$$

where  $X = [x,y,z]^T$  and  $V_w(X,t) = [u_w, v_w, w_w]^T$  are the aircraft position and wind velocity vectors expressed in the Earth-fixed inertial reference frame  $\mathcal{F}_i = \{i_1, i_2, i_3\}$ , and  $v$  and  $\omega$  are the aircraft translational and rotational velocity vectors expressed in the body-fixed reference frame,  $\mathcal{F}_b = \{b_1, b_2, b_3\}$ , respectively. Additionally, the body-fixed angular velocity components are mapped to the Euler angle rates *via*,

$$L(\Theta) = \begin{pmatrix} 1 & s\phi t\theta & s\phi t\theta \\ 0 & c\phi & -s\phi \\ 0 & s\phi\theta & t\phi sc\theta \end{pmatrix}$$

where  $t^*$  and  $sc^*$  are abbreviations for the tangent and secant trigonometric functions, respectively. The aircraft translational and rotational dynamic equations are

$$m\dot{v} = mv \times \omega + f_a(v) + mgR^T i_3 - f_{ctrl} b_3 + m\Phi v \quad (3)$$

$$I\dot{\omega} = I\omega \times \omega + m_a(\omega, v) + m_{ctrl} \quad (4)$$

where the scalar parameters,  $m$ ,  $g$ , and  $f_{ctrl}$  are the mass of the vehicle, the gravitational constant, and the control force, respectively. The aerodynamic forcing on the aircraft is modeled by the  $f_a$  vector. Furthermore,  $\Phi = R^T \frac{dV_w}{dX} R$  the spatial



wind gradient perturbing translational motion of the aircraft. Lastly,  $I$  is the moment of inertia matrix,  $m_a$  is the aerodynamic moment vector, and  $m_{\text{ctrl}}$  is the control torque vector.

To estimate wind velocity, the nonlinear, time-invariant rigid body model equations (*i.e.*, (3) and (4)) are linearized about both hovering and steady-ascending equilibrium flight. The hovering equilibrium flight condition is satisfied when  $v_{\text{eq}} \equiv \omega_{\text{eq}} \equiv 0$ . The steady ascending equilibrium flight condition is satisfied when  $v \equiv v_{\text{eq}}$ , *i.e.*,  $v_{\text{eq}} = 1 \text{ m s}^{-1}$ , and  $\omega \equiv 0$ . The linear, time-invariant (LTI) models describing the aircraft dynamics about the hovering and steady ascending equilibrium flight conditions are of the form

$$\frac{d}{dt}x = A\tilde{x} + B\tilde{u} + \Gamma w \quad (5)$$

where the vectors  $\tilde{x} = x - x_{\text{eq}}$  and  $\tilde{u} = u - u_{\text{eq}}$  denote, respectively, small deviations in the state and input vectors from their steady-state values. Additionally, the state matrix,  $A$ , models unforced dynamics, the input matrix,  $B$ , characterizes applied forcing, and the disturbance matrix,  $\Gamma$ , captures the translational kinematic effects of the wind disturbance vector,  $w = [u_w, v_w, w_w]^T$ . The state and input matrices that parameterize this model form were characterized using the system identification techniques developed by Morelli and Klein,<sup>30</sup> and have been published by González-Rocha *et al.*<sup>25</sup> Knowing the values of  $A$  and  $B$ , a state observer was synthesized to estimate wind velocity components  $u_w$  and  $v_w$  while operating in both hovering and steady-ascending equilibrium flight conditions.

**2.1.4 State observer design.** To synthesize an observer, we first reformulate eqn (5) to construct a wind-augmented model. The form of the wind-augmented model is described by,

$$\frac{d}{dt}\tilde{x}_A = \underbrace{\begin{pmatrix} A_{12} & \Gamma_{12 \times 3} \\ 0_{3 \times 12} & 0_3 \end{pmatrix}}_{A_A} \tilde{x}_w + \underbrace{\begin{pmatrix} B_{12 \times 4} \\ 0_{3 \times 4} \end{pmatrix}}_{B_A} \tilde{u} \quad (6)$$

where  $x_A = [X^T, \Theta^T, v^T, \omega^T, w^T]^T$  is the augmented state vector, and  $A_A$  and  $B_A$  are the augmented state and input matrices, respectively. This formulation assumes that the flow velocity varies slowly, relative to the system dynamics, and write  $\frac{d}{dt}w = 0$  in the wind-augmented model. Additionally, eqn (7) is the output equation describing the subset of state measurements collected on board the multirotor sUAS described in Section 2.1.2, which include the absolute position, orientation, and translational and rotational velocities.

$$y = \underbrace{\begin{pmatrix} \mathbb{I}_3 & 0_3 & 0_3 & 0_3 & 0_3 \\ 0_3 & \mathbb{I}_3 & 0_3 & 0_3 & 0_3 \\ 0_3 & 0_3 & \mathbb{I}_3 & 0_3 & \mathbb{I}_3 \\ 0_3 & 0_3 & 0_3 & \mathbb{I}_3 & 0_3 \end{pmatrix}}_{C_A} x_A \quad (7)$$

Finally, computing a suitable observer gain matrix  $G_O$ , the state of the following observer will converge to the state of the augmented system, including the wind velocity:

$$\frac{d}{dt}\hat{x}_A = A_A\hat{x}_A + B_A u + G_O(y - C_A\hat{x}_A) \quad (8)$$

More details about the observer design described in eqn (8) are provided by González-Rocha *et al.*<sup>4,25</sup>

**2.1.5 Data analysis.** Multirotor sUAS wind velocity estimates obtained hovering at 10 m AGL were processed prior to quantifying wind variations across onshore and offshore sampling locations near the surface. First, the east and north wind velocity components  $u$  and  $v$  (referred to as  $u_w$  and  $v_w$  in Sections 2.1.3 and 2.1.4) were averaged for the duration of each measurement period (approximately 2 minutes). The time-averaged wind velocity components  $\bar{u}$  and  $\bar{v}$  were then used to compute the average wind speed  $\bar{U}$  and wind direction  $\beta$  at 10 m AGL using eqn (9) and (10), respectively.

$$\bar{U} = \sqrt{\bar{u}^2 + \bar{v}^2} \quad (9)$$

$$\beta = \arctan\left(\frac{\bar{u}}{\bar{v}}\right) + 180^\circ \quad (10)$$

Wind velocity variations near the surface were then quantified as the difference between wind speed and wind direction observations measured at onshore and offshore sampling locations.

Multirotor sUAS wind velocity profiles collected at onshore and offshore sampling locations were used to quantify wind velocity variations extending from 10 to 100 m AGL. In this process,  $u$  and  $v$  wind velocity components were averaged every 10 m. The height-averaged components of wind velocity were then interpolated with respect to time and height using the bilinear interpolation function described by,

$$f(x, y) = \frac{1}{(x_2 - x_1)(y_2 - y_1)} \times [x_2 - x \quad x - x_1] \begin{bmatrix} f(x_1, y_1) & f(x_1, y_2) \\ f(x_2, y_1) & f(x_2, y_2) \end{bmatrix} \begin{bmatrix} y_2 - y \\ y - y_1 \end{bmatrix} \quad (11)$$

where  $(x_1, x_2)$  and  $(y_1, y_2)$  are the time and height interpolation domain values;  $f(x_1, y_1)$ ,  $f(x_1, y_2)$ ,  $f(x_2, y_1)$  and  $f(x_2, y_2)$  are the corresponding time and height range values; and  $x$  and  $y$  are time and height query (*i.e.*, interpolation) values. The interpolated values of  $u$  and  $v$  were then used to compute wind speed and wind direction over onshore and offshore sampling locations. Wind velocity variations from the surface to the lower atmosphere were then quantified as the difference between onshore and offshore wind speed and wind direction observations.

The multirotor sUAS wind velocity profiles were also used to quantify wind shear differences across the land-and-water interface of the lake. In our approach, we use 10 m averaged quadrotor wind speed profiles to solve for the wind shear exponent of the power law described in eqn (12)

$$\frac{\bar{U}}{\bar{U}_r} = \left(\frac{z}{z_r}\right)^\alpha \quad (12)$$





where  $\bar{U}_r$  is the averaged wind speed measured at the reference height of  $Z_r = 10$  m,  $\bar{U}$  is the averaged wind speed measured at to some height  $Z$  greater than  $Z_r$ , and  $\alpha$  is the wind shear exponent. To solve for the wind shear exponent, the wind power law was reformulated as shown in eqn (13)

$$\bar{\alpha} = \frac{1}{N-1} \sum_{i=1}^{N-1} \frac{\ln \bar{U}(i) - \ln \bar{U}_r}{\ln z(i) - \ln z_r} \quad (13)$$

where  $N - 1$  measurements of  $U$  are the average wind speed measured at every 10 m interval from 20 to 100 m AGL. The difference between exponent values corresponding to wind speed profiles collected at onshore and offshore sampling locations were then used to assess wind shear variations across the land-and-water interface of the lake.

## 2.2 Validation of multirotor sUAS wind estimation

**2.2.1 Hovering flight wind estimation performance.** On August 8th, 14 calibration flights were performed from 8:00 to 16:00 EDT at the Wright State University-Lake Campus to validate multirotor sUAS wind estimates next to an Atmos 22 sonic anemometer. The Atmos 22 sonic anemometer was installed 13

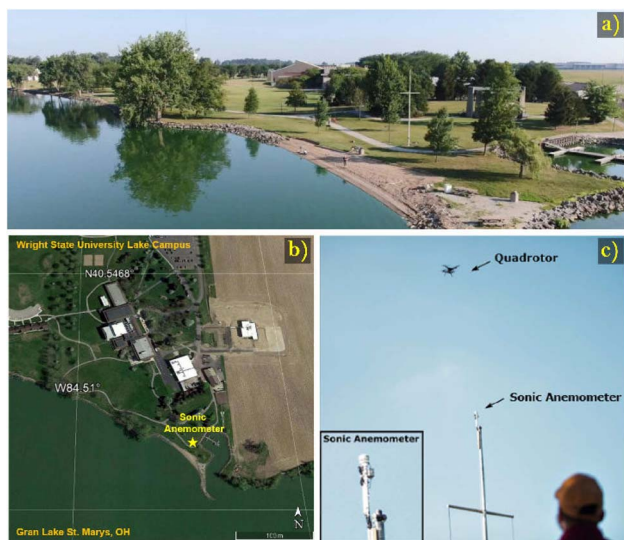


**Fig. 3** (a) An aerial view showing the landscape surrounding the location where experiments were performed to validate multirotor sUAS wind estimates hovering next to a sonic anemometer installed 13 m AGL. (b) A satellite image of Wright State University Lake Campus, Ohio where multirotor sUAS and sonic anemometer wind comparisons were performed. (c) A close-up image showing the experiment setup used to validated multirotor wind estimates next to the sonic anemometer installed 13 m AGL.

m AGL on top of a flag pole as shown in Fig. 3. The multirotor sUAS hovered 5 m away from the sonic anemometer for approximately 10 minutes prior to landing during each flight test. Multirotor sUAS wind estimates were then compared to sonic anemometer wind observations using root mean squared error (RMSE) and mean absolute error (MAE) metrics. Based on manufacturer specifications (see Table 1), the Atmos 22 sonic anemometer provides wind speed and wind direction measurements every 15 seconds with an accuracy of  $\pm 0.3$  m s<sup>-1</sup> and  $\pm 0.5^\circ$ , respectively.

**2.2.2 Steady-ascending vertical flight wind estimation.** Multirotor sUAS wind velocity profiles were also calibrated alongside a Remtech PA-0 sonic detection and ranging (SoDAR) wind profiler at the Virginia Tech Kentland Experimental Aerial Systems (KEAS) Laboratory in Blacksburg, VA on June 27th, 2019. The Remtech PA-0 SoDAR wind profiler provides wind velocity measurements from 10 m to 200 m with spatial resolution of 10 m, and a temporal resolution of 5 minutes (see Table 1). Forty-seven multirotor sUAS profiles of wind velocity were conducted from 9:00 to 21:30 EDT following at 30 minutes cadence. During each profile, the multirotor sUAS ascended vertically from 10 to 120 m AGL twice while sustaining an ascent rate of 1 m s<sup>-1</sup> (see Fig. 4). State and input measurements collected on board the quadrotor were then processed to estimate wind velocity profiles employing the wind estimation approach described in Section 2.1.3. Multirotor sUAS and



**Fig. 4** (a) A close-up image of the SoDAR wind velocity profiler used to validate multirotor sUAS wind profiles. (b) A schematic of the experiment setup used at Virginia Tech Kentland Experimental Aerial Systems Laboratory on June, 29th, 2020 to validate multirotor sUAS wind velocity profiles next to SoDAR wind profiler.

**Table 1** A summary of sonic anemometer and SoDAR performance specifications

| Make/model [m]     | Vertical range [m] | Resolution |          | Accuracy  |   |
|--------------------|--------------------|------------|----------|---|---|
|                    |                    | Spatial    | Temporal | Wind speed  | Wind direction                          |
| Meter Atmos 22 SA  | —                  | —          | 15 s     | 3% of measurement                                       | 3% of measurement                       |
| Remtech PA-0 SoDAR | 200 m              | 10 m       | 300 s    | $< \pm 0.2$ m s <sup>-1</sup> above 6 m s <sup>-1</sup> | $\pm 3^\circ$ above 2 m s <sup>-1</sup> |



SoDAR wind observations were also compared using RMSE and MAE metrics to assess the reliability of multirotor sUAS wind estimation in steady-ascending vertical flight.

## 3 Results and discussion

### 3.1 Validation of multirotor UAS wind estimates

**3.1.1 Hovering flight wind estimation.** To validate multirotor sUAS wind estimates, fourteen flights were conducted next to a sonic anemometer mounted on top of a flagpole over a 7 hour period. During this time interval, the wind magnitude varied between  $0 \text{ m s}^{-1}$  and  $4 \text{ m s}^{-1}$  as the wind direction shifted gradually from the south to the north-northeast, and between  $0 \text{ m s}^{-1}$  and  $5 \text{ m s}^{-1}$  once the wind direction became predominant from the northeast (see Fig. 5(a)). Multirotor sUAS wind inferences were found to be reliable resolving trends in diurnal wind variations based on the comparison of multirotor sUAS and sonic anemometer wind speed and wind direction observations shown in Fig. 5(a). Similar results were obtained comparing multirotor sUAS and sonic anemometer wind observations over ten-minute periods in both low and moderate

wind conditions as shown in Fig. 5(b) and (c). Additionally, multirotor sUAS observations of  $u$ ,  $v$ , and  $U$  collected from all fourteen flights were found to have MAE values of  $0.4 \text{ m s}^{-1}$ ,  $0.3 \text{ m s}^{-1}$  and  $0.4 \text{ m s}^{-1}$  and RMSE values of  $0.5 \text{ m s}^{-1}$ ,  $0.4 \text{ m s}^{-1}$  and  $0.5 \text{ m s}^{-1}$ , respectively (see Table 2), relative to sonic anemometer observations. These findings suggest that multirotor sUAS wind direction estimates are reliable across the range of wind conditions experienced during flight experiments.

**3.1.2 Steady-ascending vertical flight wind estimation.** To validate multirotor sUAS wind profiles, twenty-four flight operations were conducted next to a SoDAR wind profiler over a time span of 12 hours. A total of forty-seven wind velocity profiles were derived from the twenty three flights. Multirotor sUAS wind profiles were found to track general trends in wind speed observations based on comparisons of multirotor sUAS and SoDAR wind speed observations made at heights of 40 m, 70 m, and 100 m AGL (see Fig. 6). However, as shown in Fig. 6(b) and (c), multirotor sUAS and SoDAR wind speed observations were most consistent during the morning and evening hours. Multirotor sUAS and SoDAR wind direction measurements, on the other hand, were found to agree well throughout the duration of flight experiments (see Fig. 7). Additionally, Table 3 shows the MAE and RMSE values corresponding to multirotor sUAS measurements of  $u$ ,  $v$ , and  $U$  measured at height of 40 m, 70 m, and 100 m AGL. Overall, multirotor sUAS wind velocity profiles show a good performance inferring wind velocity ascending vertically at  $1 \text{ m s}^{-1}$  from 10 to 120 m AGL in both light and gentle breeze conditions ( $U < 6 \text{ m s}^{-1}$ ).

### 3.2 Onshore and offshore wind velocity observations

**3.2.1 Hovering flight wind observations.** Wind velocity measurements collected at onshore and offshore locations 10 m AGL on August 5th and 6th were found to vary as daytime progressed. As shown in Fig. 8, onshore and offshore wind velocity variations were predominantly characterized by wind magnitude differences (onshore and offshore wind direction remained consistent). The wind speed differences measured across onshore and offshore locations on August 5th increased from  $0 \text{ m s}^{-1}$  to  $3 \text{ m s}^{-1}$  as the wind direction shifted from south to west over a 6 hour period. On August 6th, onshore and offshore wind speed differences increased from  $0 \text{ m s}^{-1}$  to  $2 \text{ m s}^{-1}$  as the wind direction shifted gradually from the southwest to the west over a 6 hour period. The wind velocity differences measured at onshore and offshore locations on both days are likely produced by onshore and offshore roughness length and air buoyancy disparities. The roughness length

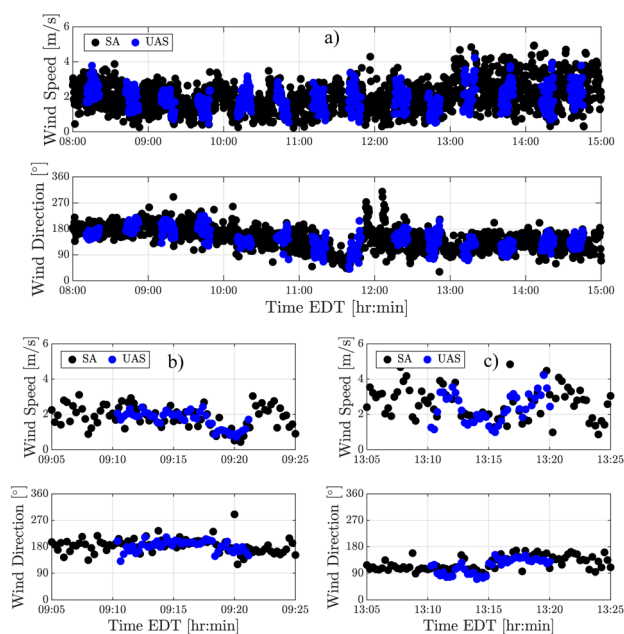
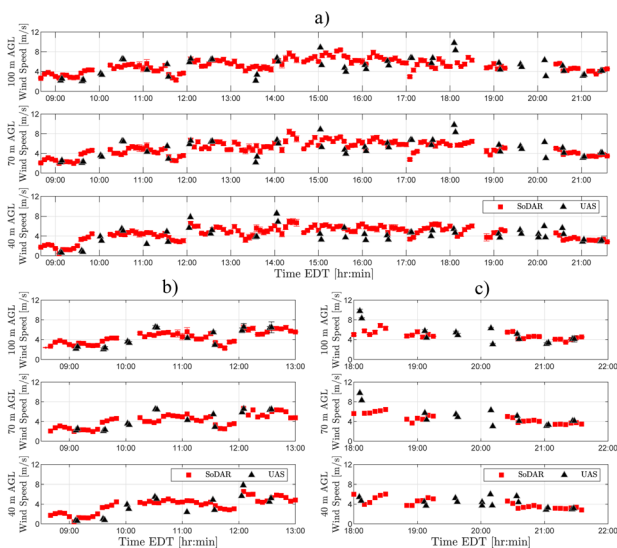


Fig. 5 Comparison plots showing the agreement between the multirotor sUAS (blue dots) and sonic anemometer (SA; black dots) measurements of wind speed and wind direction collected on August 8th from (a) 8:00 to 15:00 EDT, as well as periods of (b) light ( $U < 3 \text{ m s}^{-1}$ ) and (c) moderate ( $U < 5 \text{ m s}^{-1}$ ) wind conditions.

Table 2 Error analysis of multirotor sUAS wind velocity estimates hovering at 13 m AGL

| Height [m] | Samples | MAE                          |                              |                              | RMSE                         |                              |                              |
|------------|---------|------------------------------|------------------------------|------------------------------|------------------------------|------------------------------|------------------------------|
|            |         | $u$<br>[ $\text{m s}^{-1}$ ] | $v$<br>[ $\text{m s}^{-1}$ ] | $U$<br>[ $\text{m s}^{-1}$ ] | $u$<br>[ $\text{m s}^{-1}$ ] | $v$<br>[ $\text{m s}^{-1}$ ] | $U$<br>[ $\text{m s}^{-1}$ ] |
| 13         | 577     | 0.4                          | 0.3                          | 0.4                          | 0.5                          | 0.4                          | 0.6                          |





**Fig. 6** (a) A comparison plot showing the agreement between multirotor sUAS (black) and SoDAR (red) wind speed observations collected at 40 m, 70 m, and 100 m AGL on June 27th, 2020. The multirotor sUAS and SoDAR wind speed observations were found in closer agreement during the (b) morning and (c) evening sampling periods.

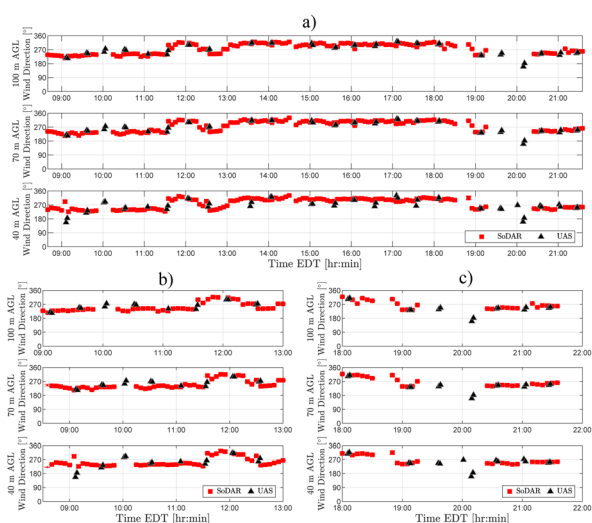


**Fig. 7** (a) A comparison plot showing the agreement between multirotor sUAS (black) and SoDAR (red) wind direction observations collected at 40 m, 70 m, and 100 m AGL on June 27th, 2020. Multirotor and SoDAR wind direction observations were found in good agreement consistently during the (b) morning and (c) evening sampling periods.

**Table 3** Error analysis of multirotor sUAS wind velocity profiles

| Height [m] | Samples | MAE                       |                           |                           | RMSE                      |                           |                           |
|------------|---------|---------------------------|---------------------------|---------------------------|---------------------------|---------------------------|---------------------------|
|            |         | $u$ [ $\text{m s}^{-1}$ ] | $v$ [ $\text{m s}^{-1}$ ] | $U$ [ $\text{m s}^{-1}$ ] | $u$ [ $\text{m s}^{-1}$ ] | $v$ [ $\text{m s}^{-1}$ ] | $U$ [ $\text{m s}^{-1}$ ] |
| 40         | 40      | 1.1                       | 1.6                       | 2.0                       | 1.6                       | 2.1                       | 2.6                       |
| 70         | 39      | 1.2                       | 1.5                       | 1.9                       | 1.8                       | 1.8                       | 2.5                       |
| 100        | 39      | 1.2                       | 1.5                       | 1.9                       | 1.8                       | 1.8                       | 2.5                       |
| Average    |         | 1.2                       | 1.5                       | 1.9                       | 1.7                       | 1.9                       | 2.5                       |

alone is estimated to be approximately 100 times larger onshore.

### 3.3 Steady-ascending vertical flight wind observations

Wind velocity profiles collected on August 5th and 6th show that onshore and offshore wind velocity variations aloft change with respect to time and height. On both days, as shown in Fig. 9(a) and 10(a), the onshore and offshore wind speed differences measured from 10 m to 80 m AGL were found to increase significantly over time. Wind speed differences measured across onshore and offshore locations were more pronounced near the ground, where roughness length and buoyancy flow effects are most significant. Wind velocity variations associated with onshore and offshore wind direction differences were observed to be less consistent. On August 5th, notable differences were found between onshore and offshore wind direction measurements collected during the middle of the day. However, the measurements collected during this period were fewer in comparison to measurements collected during early-morning and late-afternoon hours (see Fig. 9(a)). On August 6th, as shown in Fig. 10(a), wind direction differences across onshore and offshore locations were observed to remain small with respect to time and height.

Considerable wind velocity variations were also observed across onshore and offshore locations based on wind shear characterizations derived from vertical profiles collected on August 5th and 6th. As shown in Fig. 11, onshore and offshore wind shear differences grew significantly larger as wind speed increased with time on August 6th. Wind shear differences measured across onshore and offshore locations were less pronounced as wind speed increased with time to a lesser degree on August 5th. On both days, however, onshore and offshore wind shear trends were found to be largely consistent over time. These results further demonstrate the capability of multirotor sUAS wind sensing for characterizing wind velocity variations in aquatic environments.

### 3.4 Discussion

Results from the multirotor sUAS wind sensing operations at Grand Lake St. Marys, Ohio revealed significant wind velocity variations at 10 m AGL between onshore and offshore sampling locations. Wind speed observations measured offshore were generally higher compared to the wind speed observations measured over water (see Fig. 8). Additionally, wind speed differences across onshore and offshore locations were observed to increase during afternoon hours as southerly





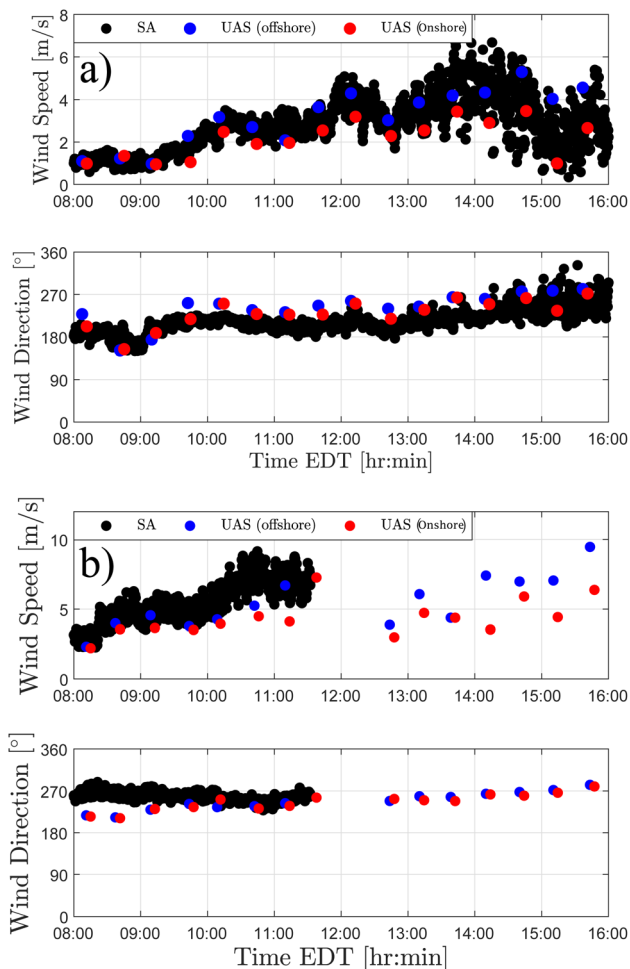


Fig. 8 Comparison plots showing differences between multirotor sUAS estimates of wind speed and wind direction at onshore (red) and offshore (blue) locations 10 m AGL on the (a) 5th and (b) 6th of August. The black markers correspond to the sonic anemometer (SA) observations collected 13 m AGL on August 5th and 6th.

(onshore) winds subsided and westerly (alongshore) winds strengthened. Wind direction observations, on the other hand, varied uniformly between onshore and offshore locations as wind direction shifted from south to west, resulting in small wind direction difference over time. Therefore, 10 m wind velocity variations observed across onshore and offshore sampling locations were characterized in large part by wind speed differences. The wind speed differences observed across onshore and offshore locations were likely driven by surface roughness length and air buoyancy effects, which are expected to be more pronounced when the wind is blowing parallel to the shoreline.

The quadrotor wind velocity profiles collected at Grand Lake St. Marys also show wind variations across land and water to increase significantly from 10 to 100 m AGL as daytime evolves. Wind velocity profiles show wind speed trends to be consistent with observations measured at 10 m AGL—wind speeds were increasingly higher over water compared to land (see Fig. 9 and 10). Similarly, onshore and offshore wind velocity profiles show

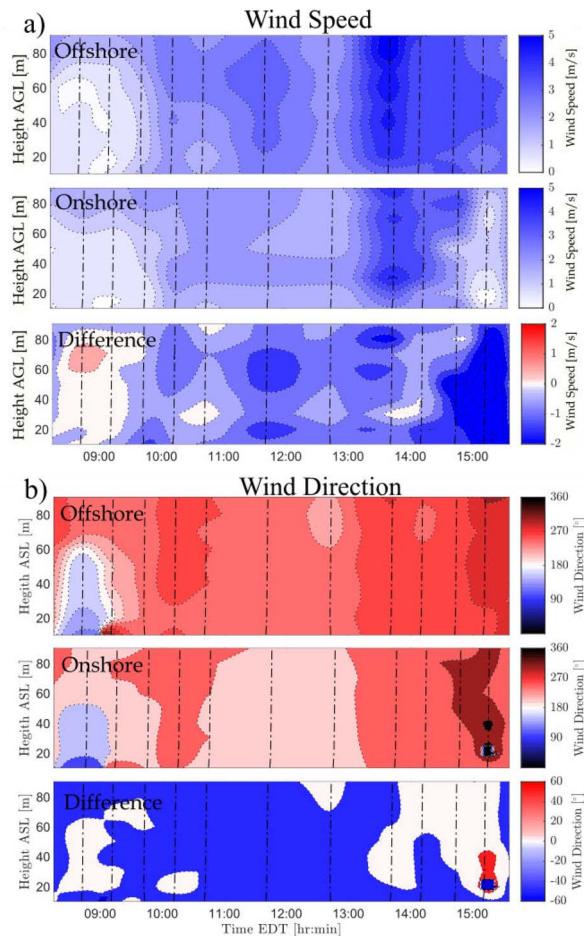


Fig. 9 2-D contour plots showing the comparison of onshore and offshore profiles of (a) wind speed and (b) wind direction measured on August 5th. The dashed lines show the sUAS flights.

wind direction to vary uniformly with time. Additionally, the characterization of wind shear based on quadrotor wind velocity profiles show wind speed shear to be greater onshore. These observations are consistent with expected outcomes given that surface roughness and heat flux effects are considerably smaller over water.

Multirotor sUAS wind estimates were also found to be reliable resolving wind velocity trends based on validation experiments performed next to *in situ* and remote atmospheric sensors. Results from the 14 flight operations next to a sonic anemometer installed 13 m AGL showed multirotor sUAS and sonic anemometer measurements of wind speed and wind direction to track well during periods of light and moderate wind conditions. The comparison of 45 multirotor wind velocity profiles and SoDAR observations also demonstrate multirotor sUAS wind estimates to be reliable resolving wind velocity variations across space and time in both light and moderate conditions. Larger wind speed errors observed during afternoon hours are likely the result of model-based wind estimation limitations. The validity of the linear approximation described in eqn (5) may be exceeded in strong wind conditions (*i.e.*,  $U > 6 \text{ m s}^{-1}$ ). These results are consistent with previous calibration





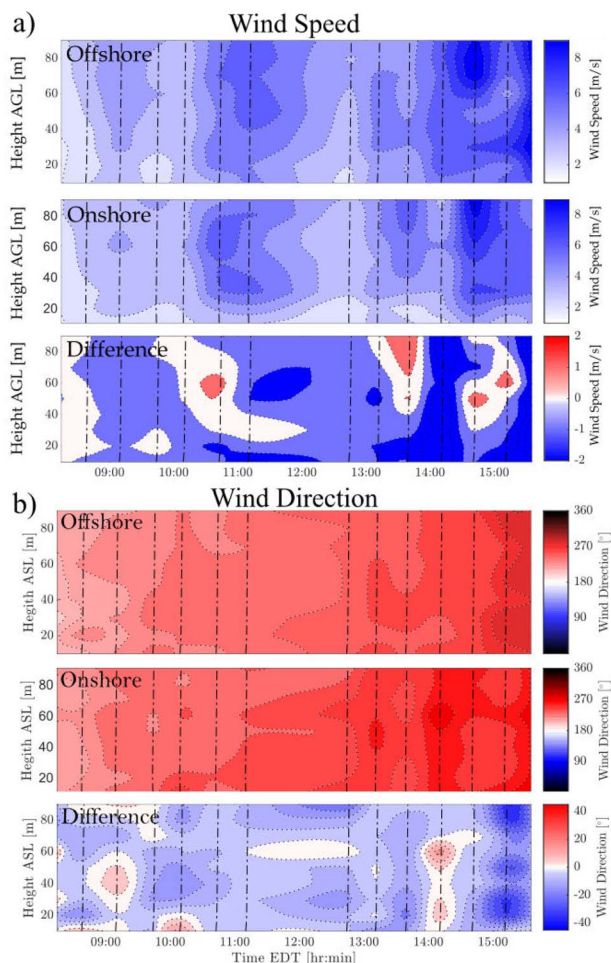


Fig. 10 2-D contour plots showing the comparison of onshore and offshore profiles of (a) wind speed and (b) wind direction measured on August 6th. The dashed lines show the sUAS flights.

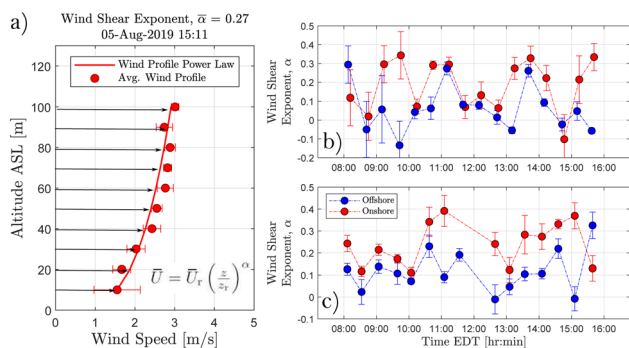


Fig. 11 (a) A schematic showing a 10 m averaged wind profile and corresponding onshore wind shear estimate derived from the power law formulation described eqn (13). (b) A comparison plot showing how the onshore offshore wind shear exponents derived from multirotor sUAS wind profiles performed on August 5th, 2019 varied with time. (c) A comparison plot showing how the onshore offshore wind shear exponents derived from multirotor sUAS wind profiles performed on August 6th, 2019 varied with time.

experiments performed alongside *in situ* remote sensing instruments.<sup>4,6,25</sup> Therefore, multirotor sUAS wind estimates derived from both hovering and steady ascending flight operations can provide reliable observations of atmospheric flows in aquatic environments with some restrictions. Moreover, these calibration results extend the drone-based measurements presented by Bilyeu *et al.*<sup>28</sup> and González-Rocha *et al.*<sup>7</sup> where wind velocity estimates were obtained while hovering, and highlight the potential of drone-based wind profiles for characterizing aerosolization processes in splash zones.<sup>31</sup>

Technology improvements are also necessary to increase the effectiveness of multirotor sUAS wind sensing capabilities. Currently, the persistence of multirotor sUAS flight operations is limited by the aircraft performance envelop and battery technology, as well as the accessibility to battery charging stations. During field experiments, flight operations were constrained to a 30 minutes cadence due to having a limited number of batteries (see Fig. 8). Weather conditions also constrain the persistence of wind sensing flight operations as it is not safe to fly multirotor sUAS in rain or high wind events, both operating autonomously or with a human in the loop. For this reason, flight operations were paused during rainstorm events that took place between 11:00 and 12:30 on August 7th (see Fig. 10). Moreover, reliable wind estimates depend on accurate dynamic models. Therefore, airframe modifications performed after the completion of the LTI model characterization will likely increase the wind measurement error. Some of these constraints will become less significant as multirotor sUAS performance, battery technology, and real-time parameter estimation improves with time.

Overall, the multirotor sUAS capabilities we have presented for measuring atmospheric flow variations in aquatic environments are an important step toward understanding the atmospheric transport of hazardous agents. For instance, multirotor sUAS wind sensing capabilities paired with particle counting and water sampling technology can help characterize the aerosolization of toxic cyanobacteria produced by harmful algal blooms such as the ones found in Grand Lake St. Marys in different seasons.<sup>28,29,32–36</sup> Moreover, vertical wind velocity and particle count information collected both hovering and steadily ascending provide new possibilities for validating atmospheric dispersion models that are used to quantify exposure to aerosol emissions. To date, atmospheric dispersion models have only been validated using near-ground observations.<sup>37–40</sup> Lastly, the spatiotemporal resolution of wind velocity that multirotor sUAS provide is also critical for developing intelligent advisory systems that can help downwind communities rapidly and effectively detect and respond to hazardous exposure events.

## 4 Conclusions

In this paper, we explore the application of multirotor sUAS for characterising atmospheric flow variations across land and water in aquatic environments using a model-based wind estimation algorithm. Field study results show that microscale atmospheric flows can vary significantly over short distances where land and water interface. Additionally, experiments



conducted next to *in situ* and remote sensing instruments demonstrate multirotor sUAS to be reliable measuring wind velocity trends both in hovering and steady ascending flight. Therefore, further development of multirotor sUAS atmospheric sensing capabilities are imperative for increasing the resolution of atmospheric observations in aquatic environments. High-fidelity meteorological measurements, along with accurate aerosol concentration counts, can improve atmospheric transport predictions. Improved atmospheric transport predictions can lead to more effective advisory systems and fewer exposure events.

## Author contributions

J. G. R. lead the conceptualization, data curation, formal analysis, investigation, methodology, validation, visualization, and writing of the original manuscript draft. L. B. supported data curation, investigation, and reviewing and editing the original draft. S. D. R. and H. F. contributed to the conceptualization, data curation, investigation, and reviewing and editing of manuscript draft. S. J. J. supported funding acquisition, project administration efforts, provided resources, and reviewed and edited the original manuscript draft. A. A. supported funding acquisition, project administration efforts, and reviewed and edited the original manuscript draft. D. G. S. lead funding acquisition and project administration efforts, and contributed to conceptualization, data curation, investigation, and reviewing and edition of original manuscript draft.

## Conflicts of interest

There are no conflicts to declare.

## Acknowledgements

This research was supported in part by the Institute for Critical Technology and Applied Science at Virginia Tech under grant number (ICTAS-178429).

## Notes and references

- 1 K. Barskov, R. Chernyshev, V. Stepanenko, I. Repina, A. Y. Artamonov, S. Guseva and A. Gavrikov, *IOP Conference Series: Earth and Environmental Science*, 2017, p. 012003.
- 2 K. Barskov, V. Stepanenko, I. Repina, A. Artamonov and A. Gavrikov, *Boundary-Layer Meteorology*, 2019, **173**, 311–320.
- 3 M. Varentsov, V. Stepanenko, I. Repina, A. Artamonov, V. Bogomolov, N. Kuksova, E. Marchuk, A. Pashkin and A. Varentsov, *Atmosphere*, 2021, **12**, 380.
- 4 J. González-Rocha, C. A. Woolsey, C. Sultan and S. F. De Wekker, *J. Guid. Control Dyn.*, 2019, **42**, 836–852.
- 5 P. J. Nolan, J. Pinto, J. González-Rocha, A. Jensen, C. N. Vezzi, S. C. Bailey, G. De Boer, C. Diehl, R. Laurence, C. W. Powers, H. Foroutan, S. D. Ross and D. G. Schmale III, *Sensors*, 2018, **18**, 4448.
- 6 L. Barbieri, S. T. Kral, S. C. C. Bailey, A. E. Frazier, J. D. Jacob, J. Reuder, D. Brus, P. B. Chilson, C. Crick, C. Detweiler, A. Doddi, J. Elston, H. Foroutan, J. González-Rocha, B. R. Greene, M. I. Guzman, A. L. Houston, A. Islam, O. Kemppinen, D. Lawrence, E. A. Pillar-Little, S. D. Ross, M. P. Sama, I. Schmale, G. David, T. J. Schuyler, A. Shankar, S. W. Smith, S. Waugh, C. Dixon, S. Borenstein and G. de Boer, *Sensors*, 2019, **19**, 2179.
- 7 J. González-Rocha, A. J. Sosa, R. Hanlon, A. A. Allen, I. Rypina, D. G. Schmale-III and S. D. Ross, *Appl. Ocean Res.*, 2021, **110**, 102538.
- 8 T. G. Konrad, M. L. Hill, J. R. Rowland and J. H. Meyer, *Johns Hopkins APL Tech. Dig.*, 1970, **10**, 11–21.
- 9 J. W. Langelaan, N. Alley and J. Neidhoefer, *J. Guid. Control Dyn.*, 2011, **34**, 1016–1030.
- 10 P. J. Nolan, H. G. McClelland, C. A. Woolsey and S. D. Ross, *Sensors*, 2019, **19**, 1607.
- 11 H. G. McClelland and C. A. Woolsey, *J. Guid. Control Dyn.*, 2020, **43**, 1069–1081.
- 12 J. Elston, B. Argrow, M. Stachura, D. Weibel, D. Lawrence and D. Pope, *J. Atmos. Ocean. Technol.*, 2015, **32**, 97–115.
- 13 P. Abichandani, D. Lobo, G. Ford, D. Bucci and M. Kam, *IEEE Access*, 2020, **8**, 54910–54927.
- 14 C. A. Wolf, R. P. Hardis, S. D. Woodrum, R. S. Galan, H. S. Wichelt, M. C. Metzger, N. Bezzo, G. C. Lewin and S. F. de Wekker, *2017 Systems and Information Engineering Design Symposium (SIEDS)*, 2017, pp. 32–37.
- 15 T. Shimura, M. Inoue, H. Tsujimoto, K. Sasaki and M. Iguchi, *J. Atmos. Ocean. Technol.*, 2018, **35**, 1621–1631.
- 16 G. W. Donnell, J. A. Feight, N. Lannan and J. D. Jacob, *2018 Atmospheric Flight Mechanics Conference*, 2018, p. 2986.
- 17 C. Ingenhorst, G. Jacobs, L. Stößel, R. Schelenz and B. Juretzki, *Wind Energy Sci.*, 2021, **6**, 427–440.
- 18 S. Prudden, A. Fisher, M. Marino, A. Mohamed, S. Watkins and G. Wild, *J. Wind Eng. Ind. Aerodyn.*, 2018, **176**, 197–210.
- 19 N. Vasiljević, M. Harris, A. Tegtmeier Pedersen, G. Rolighed Thorsen, M. Pitter, J. Harris, K. Bajpai and M. Courtney, *Atmos. Meas. Tech.*, 2020, **13**, 521–536.
- 20 P. P. Neumann and M. Bartholmai, *Sens. Actuators, A*, 2015, **235**, 300–310.
- 21 C. Brosy, K. Krampf, M. Zeeman, B. Wolf, W. Junkermann, K. Schäfer, S. Emeis and H. Kunstmann, *Atmos. Meas. Tech.*, 2017, **10**, 2773–2784.
- 22 R. T. Palomaki, N. T. Rose, M. van den Bossche, T. J. Sherman and S. F. De Wekker, *J. Atmos. Ocean. Technol.*, 2017, **34**, 1183–1191.
- 23 T. M. Bell, B. R. Greene, P. M. Klein, M. Carney and P. B. Chilson, *Atmos. Meas. Tech.*, 2020, **13**, 3855–3872.
- 24 M. J. Brewer and C. B. Clements, *Fire*, 2020, **3**, 36.
- 25 J. González-Rocha, S. F. De Wekker, S. D. Ross and C. A. Woolsey, *Sensors*, 2020, **20**, 1341.
- 26 A. Shelekhov, A. Afanasiev, E. Shelekhova, A. Kobzev, A. Tel'minov, A. Molchunov and O. Poplevina, *Drones*, 2022, **6**, 1–22.
- 27 S. A. Bollt and G. P. Bewley, *J. Fluid Mech.*, 2021, **921**, A18.
- 28 L. Bilyeu, B. Bloomfield, R. Hanlon, J. González-Rocha, S. J. Jacquemin, A. Ault, J. Birbeck, J. Westrick, H. Froutan, L. Marr, S. Ross, C. Powers and D. G. Schmale III, *Environ. Sci.: Atmos.*, 2022, 1351.



- 29 R. Hanlon, S. J. Jacquemin, J. A. Birbeck, J. A. Westrick, C. Harb, H. Gruszewski, A. P. Ault, D. T. Scott, H. Foroutan, S. D. Ross, J. González-Rocha, C. Powers, L. Pratt, H. Looney, G. Baker and D. G. Schmale III, *Frontiers in Remote Sensing*, 2022, 949052.
- 30 E. A. Morelli and V. Klein, *Aircraft System Identification: Theory and Practice*, Sunflyte Enterprises, Williamsburg, Virginia, 2016.
- 31 R. B. Pietsch, H. Grothe, R. Hanlon, C. W. Powers, S. Jung, S. D. Ross and D. G. Schmale III, *PeerJ*, 2018, **6**, e5663.
- 32 D. G. Schmale III, A. P. Ault, W. Saad, D. T. Scott and J. A. Westrick, *Front. Bioeng. Biotechnol.*, 2019, **7**, 128.
- 33 N. E. Olson, M. E. Cooke, J. H. Shi, J. A. Birbeck, J. A. Westrick and A. P. Ault, *Environ. Sci. Technol.*, 2020, **54**, 4769–4780.
- 34 N. E. Olson, N. W. May, R. M. Kirpes, A. E. Watson, K. D. Hajny, J. H. Slade, P. B. Shepson, B. H. Stirm, K. A. Pratt and A. P. Ault, *ACS Earth Space Chem.*, 2019, **3**, 2765–2774.
- 35 H. E. Plaas and H. W. Paerl, *Environ. Sci. Technol.*, 2020, **55**, 44–64.
- 36 S. D. Ross, J. Fish, K. Moeltner, E. M. Bollt, L. Bilyeu and T. Fanara, *Harmful Algae*, 2022, **111**, 102149.
- 37 D. E. Aylor and T. K. Flesch, *J. Appl. Meteorol. Climatol.*, 2001, **40**, 1196–1208.
- 38 N. S. Holmes and L. Morawska, *Atmos. Environ.*, 2006, **40**, 5902–5928.
- 39 R. R. Thiruvengkatachari, V. Carranza, F. Ahangar, A. Marklein, F. Hopkins and A. Venkatram, *Agric. For. Meteorol.*, 2020, **290**, 108011.
- 40 R. R. Thiruvengkatachari, Y. Ding, D. Pankratz and A. Venkatram, *Air Qual., Atmos. Health*, 2022, **15**, 363–372.

